I&EC research
Industrial & Engineering Chemistry Research
pubs.acs.org/IECR
Article

Fixed Bed Adsorption of CO_2, CH_4, and N_2 and Their Mixtures in Potassium-Exchanged Binder-Free Beads of Y Zeolite

Ezzeldin Aly, Lucas F.A.S. Zafanelli,* Adriano Henrique, Marcella Golini Pires, Alírio E. Rodrigues, Kristin Gleichmann, and José A.C. Silva*

Cite This: *Ind. Eng. Chem. Res.* 2021, 60, 15236−15247

Read Online

ACCESS | Metrics & More | Article Recommendations | Supporting Information

ABSTRACT: The adsorption of carbon dioxide (CO_2), methane (CH_4), and nitrogen (N_2) has been studied on potassium-exchanged (95%) binder-free beads of Y zeolite through single, binary, and ternary fixed bed breakthrough experiments, covering the temperature range between 313 and 423 K and a pressure of up to 350 kPa. At 313 K and 350 kPa, the single-component data obtained showed that the amounts adsorbed of CO_2, CH_4, and N_2 are around 6.42, 1.45, and 0.671 mol kg^{-1}, respectively. The binary experiments CO_2/N_2 carried out under typical post-combustion conditions show a selectivity of CO_2 over N_2 around 104. The ternary experiments resulted in the selectivities of CO_2 over CH_4 and N_2 around 19 and 45, respectively. The adsorption equilibrium data have been modeled by the dual-site Langmuir model, and the breakthrough experiments were numerically simulated with a suitable dynamic fixed bed adsorption model. The model predicts with good accuracy the systematic behavior of all breakthrough experiments. The results shown in the present work prove that the potassium-exchanged binder-free beads of Y zeolite enhance the amount adsorbed of CO_2 at low partial pressure over other alkali metal-exchanged faujasites and efficiently separate it from binary (CO_2/N_2) and ternary (CO_2/CH_4/N_2) mixtures by fixed bed adsorption.

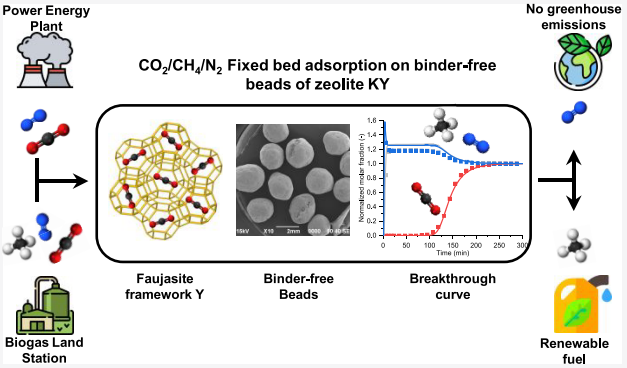

INTRODUCTION

The generation of carbon dioxide is inherent in the combustion of fossil fuels, and the efficient capture of CO_2 from industrial operations is regarded as an important strategy to achieve a significant reduction in atmospheric CO_2 levels.[1−9] Post-combustion capture is referred to as the capture of CO_2 from flue gases produced by the combustion of carbon-based fuels, such as coal[10] or natural gas. It is a crucial capture route as it provides means of CO_2 capture for new and existing combustion technologies without encountering any technological risks or radical changes.[11−13] Adsorption processes are promising capture technologies as they can use specific adsorbents by acting in the limit as molecular sieves to separate CO_2 from other flue gas constituents. Physical adsorbents such as zeolites are safe for the local environment and generally inexpensive to manufacture and scale-up.[12,14]

Major challenges that face post-combustion CO_2 capture technology by adsorption include the low pressure of flue gas (101.3 kPa) and the difficulty to separate the relatively low concentration of CO_2 (10−15%) from the large amounts of nitrogen.[3,15] Processes for removing CO_2 from CH_4 are also important for upgrading both renewable and non-renewable energy sources such as landfill gas, biogas, and natural gas.[16−20] These gases contain significant amounts of methane (50 vol %) balanced by carbon dioxide, nitrogen, and other contaminants that have to be removed before liquefaction to meet pipeline grade specifications.[21,22]

Adsorption-based gas separations are currently being used to separate CO_2 from mixtures containing CO_2/N_2 and CO_2/CH_4/N_2 for several applications.[23−26] Metal−organic frameworks (MOFs) are considered a new class of adsorbents with great future potential for CO_2 capture due to their high surface area and pore volume.[27] However, MOFs need to be further refined regarding their production in large-scale, chemical, and thermal stability, which are properties already well established in zeolites.[24] Conventional zeolites such as 13X, 4A, and 5A forms are known as having excellent properties to adsorb large amounts of CO_2 while having high CO_2 selectivity in comparison to CH_4 and N_2.[6,24−26,28−30]

Zeolites Y and X belong to the family of aluminosilicate molecular sieves with a faujasite-type structure (FAU), being

Received: June 11, 2021
Revised: September 16, 2021
Accepted: October 4, 2021
Published: October 13, 2021

https://doi.org/10.1021/acs.iecr.1c02261
Ind. Eng. Chem. Res. 2021, 60, 15236−15247

different only by the Si/Al atomic ratio (1.5−3.0 for NaY compared to 1.0−1.5 for NaX).[31,32] Barrer and Gibbons[33] pioneered the concept of ion exchange by investigating the properties of zeolitic carbon dioxide in different intracrystalline environments in faujasites (Linde Sieve X). It was found that such adsorbents reveal different behaviors and trends based on the modification of the intracrystalline environment through ion exchange. Furthermore, Walton *et al.*[34] and Pirngruber *et al.*[35] have performed studies to examine the CO_2 adsorption on Y and X zeolites modified by alkali metal cation exchange of a parent Na sample. Both studies agree that CO_2 adsorption is influenced by diverse structural characteristics of zeolites such as cation size, acid−base surface properties, size of the pores, number of exchangeable cations, polarizing power, distribution, and Si/Al ratio (details provided in Section S1 of the Supporting Information).[36−39]

By considering all these factors, it is possible to tune the adsorptive properties of zeolites by ion exchange to optimize the most suitable material that enriches substantially the CO_2 adsorption for a specific process. Moreover, zeolite production is well established being an advantage compared to other types of adsorbents to a fast application as they are used industrially for more than 60 years.[40] Furthermore, the development of binder-free zeolite adsorbents has proven to increase the adsorption capacity up to 20%.[24−26,30,41,42]

Experimental and theoretical studies concerning the adsorption of CO_2, CH_4, and N_2 and their mixtures in potassium-exchanged Y zeolite (KY) lack information in the literature. Accordingly, this work aims to investigate by a series of fixed bed breakthrough experiments the adsorption of single, binary, and ternary mixtures of $CO_2/CH_4/N_2$ in binder-free beads of KY zeolite, at temperatures of 313, 373, and 423 K and a total pressure of up to 350 kPa (under compositions typical of post-combustion and biogas upgrading processes). From the data, the single- and multicomponent adsorption equilibrium isotherms were collected and fitted with the single and dual-site Langmuir isotherms. A suitable mathematical model including axial dispersion, mass transfer resistances, and heat effects was also developed and applied to describe and predict numerically the overall dynamics of the experiments. Performance metrics such as selectivities and working capacities were also evaluated. At the same time, the experimental data collected is compared with an already available one in the literature for other ion-exchanged X and Y faujasite zeolites.

MATERIALS AND METHODS

Adsorbent and Adsorbate. The potassium-exchanged (95%) Y zeolite studied in this work was synthesized in the binder-free form in the labs of Chemiewerk Bas Köstritz GmbH (Germany). The bead particle diameter ranges between 1.6 and 2.5 mm. The exchange started from a commercial type of the binder-free Y sodium zeolite form (Köstrolith NaYBFK) with a Si/Al ratio of 2.5 to achieve the 95% potassium exchange degree value.

Air Liquide supplied the adsorbate and inert gases with the following specifications: He ALPHAGAZ 2 (99.9998%), CO_2 N48 (99.998%), CH_4 N35 (99.95%), and N_2 N50 (99.999%).

Characterization. The porous nature of the binder-free zeolite KY was accessed by nitrogen adsorption−desorption at 77 K and a pressure of up to 101.3 kPa using an accelerated surface area and porosimetry system (Micrometrics ASAP 2020 V4.02). Before the experiments, the sample was outgassed at 573 K for 12 h in a vacuum atmosphere.

The porosity of the materials was evaluated by mercury intrusion porosimetry, performed in a pore size analyzer (Micromeritics AutoPore IV 9500), covering the pressure range between 0.003 and 207 MPa, after activation in the same previously described conditions.

The surface morphology of the binder-free zeolite KY was analyzed using a scanning electron microscopy instrument (JEOL Model JSM-6490) with a high resolution of 3.0 nm.

All the characterization studies were performed at the Laboratorio de Sólidos Porosos of Málaga University.

Experimental Procedure. A homemade single- and multicomponent breakthrough apparatus was used to study the fixed bed adsorption of CO_2, CH_4, and N_2 and their binary/ternary mixtures. This apparatus was used in previous works[41] and is illustrated in Figure S1 of the Supporting Information. Table S1 shows the properties of the adsorbent and column used in the experiments performed through this work.

The experimental system consists of three main sections, namely, the gas preparation section, adsorption column system, and an analytical system using a thermal conductivity detector (TCD) gas chromatograph (SRI 8610C - Gas Chromatograph equipment, USA).

In the gas preparation section, the partial pressure of the adsorbable species was set-up before being introduced in the adsorption column. In the adsorption section, the mixture passes through the adsorption column that is placed inside a temperature-controlled oven. Mass flow controllers (Alicat MFCs, USA) were used to set-up the flow rates of both carrier gas (He) and adsorbate gases ($CO_2/CH_4/N_2$), and an electronic back-pressure controller (Alicat BPR, USA) was used to establish the total pressure of the system. For single-component experiments, the column gas outlet goes directly to the TCD detector. For binary and ternary experiments, the column gas outlet passes through a six-port VICI-Valco valve gas trapping loop system. This valve was programmed to inject the mixture sample, trapped in the loop, into a gas chromatographic column (HayeSep packed column) at a fixed time step. The species were separated in less than 1 min and analyzed by the TCD-GC system. Before the first run, the adsorption column was activated for 12 h at 623 K under vacuum and pure helium flow (10 mL min^{-1}) to remove any pre-absorbed undesirable components, such as water.

In chromatographic breakthrough experiments, the adsorption equilibrium concentration is calculated by integrating the molar flow profiles of the breakthrough curves by using the following equation:[43]

$$q_{\mathrm{exp},i} = \frac{1}{m_{\mathrm{ads}}}\left(F_{\mathrm{f},i}t_n - \int_0^{t_\infty} F_i \, \mathrm{d}t - \varepsilon_{\mathrm{b}} V_{\mathrm{c}} C_{0i}\right) \quad (1)$$

where $q_{\mathrm{exp},\,i}$ is the experimental measured adsorption equilibrium concentration, m_{ads} is the adsorbent mass in the column, $F_{\mathrm{f},\,i}$ is the feed molar flow rate of component i at the inlet of the fixed bed, F_i is the molar flow rate of component i at the outlet of the fixed bed, t_∞ is the saturation time, ε_{b} is the bed porosity, V_{c} is the adsorption column volume, and C_{0i} is the feed gas-phase concentration of component i at the inlet of the fixed bed.

Adsorption Equilibrium Model. The dual-site Langmuir (DSL) model isotherm distinguishes two categories of sorption

https://doi.org/10.1021/acs.iecr.1c02261
Ind. Eng. Chem. Res. 2021, 60, 15236−15247

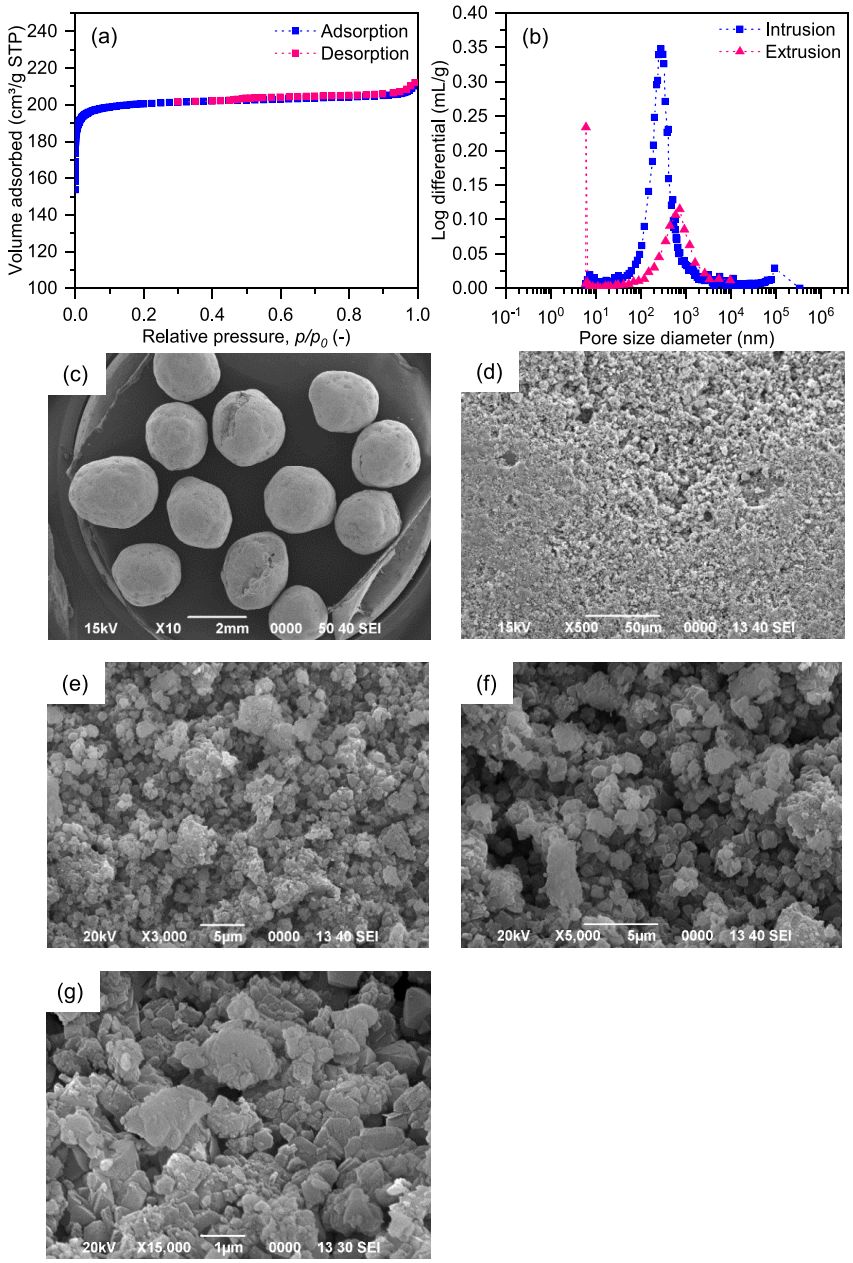

Figure 1. Characterizations: (a) adsorption equilibrium isotherm of N_2 at 77 K on binder-free zeolite KY; (b) differential intrusion and extrusion of Hg in pores on binder-free zeolite KY; SEM images of binder-free zeolite KY at (c) 10×, (d) 500×, (e) 3000×, (f) 5000×, and (g) 15,000×.

sites in the adsorbent, each following the Langmuir model assumption, with different binding energies and maximum adsorption capacities.[43,44] The extended DSL isotherm for a multicomponent system is

$$q_i = q_{m1,i}\frac{b_{1i}p_i}{1 + \sum_{i=1}^{n} b_{1i}p_i} + q_{m2,i}\frac{b_{2i}p_i}{1 + \sum_{i=1}^{n} b_{2i}p_i} \quad (2)$$

where q_i is the adsorbed equilibrium concentration, p_i is the partial pressure of sorbate, and q_{mi} and b_i are the maximum adsorbed equilibrium concentration and the adsorption affinity constant of each site, respectively. The subscripts 1 and 2 indicate the two types of sorption sites, the index i refers to the sorbate species, and n refers to the number of components present in the mixture. This model deviates from the ideal Langmuir model accounting for the heterogeneity of the adsorbent surface due to possible different adsorption site locations on the faujasite framework. It reverts to the Langmuir model if considering only one equivalent energy site.

The effect of temperature on the adsorption affinity constant, b_i, follows a van't Hoff equation

$$b_i = b_{\infty,i}e^{(-\Delta H_i/RT)} \quad (3)$$

where $b_{\infty,i}$ is the pre-exponential factor of the affinity constant, R is the ideal gas constant, $(-\Delta H_i)$ is the heat of adsorption, and T is the temperature.

Isosteric Heats. The isosteric heat can give us an idea of the heterogeneity of the adsorption surface, and its dependence as a function of the adsorbed equilibrium concentration can give us an indication of the contribution of adsorbate−adsorbent interactions.[35] The isosteric heat (ΔH_{st}) as a function of the adsorbed equilibrium concentration is defined by the following equation[45]

https://doi.org/10.1021/acs.iecr.1c02261
Ind. Eng. Chem. Res. 2021, 60, 15236−15247

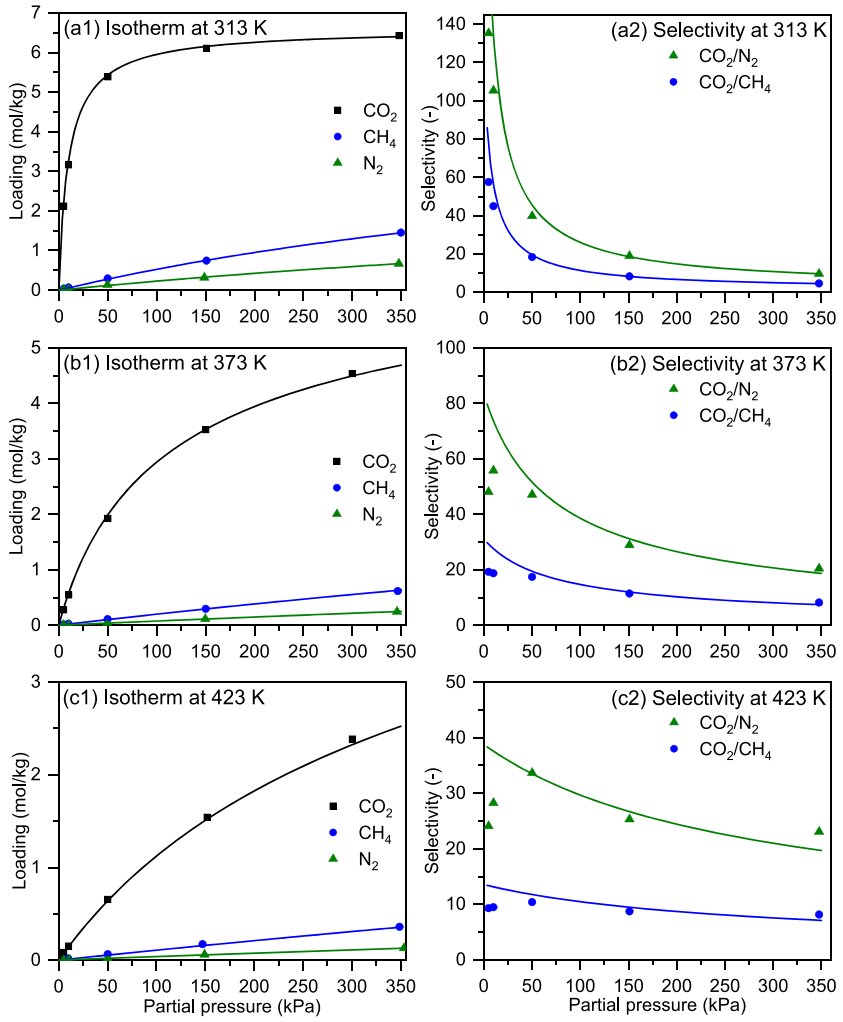

Figure 2. Adsorption equilibrium isotherms of CO_2, CH_4, and N_2 at (a1) 313, (b1) 373, and (c1) 423 K in binder-free zeolite KY; selectivity of CO_2/N_2 and CO_2/CH_4 at (a2) 313, (b2) 373, and (c2) 423 K in binder-free zeolite KY. Experimental = symbols; numerical = lines.

$$\frac{\Delta H_{st}}{RT^2} = -\left(\frac{\partial \ln p}{\partial T}\right)_q \tag{4}$$

Assuming that ΔH_{st} is independent of the temperature, the isosteric heat can be calculated directly from the experimental adsorption isotherms by integrating eq 4 at a fixed coverage in a plot of $\ln p$ against $1/T$[31]

$$\ln p = \text{constant} - \frac{\Delta H_{st}}{RT} \tag{5}$$

It can be also predicted or calculated numerically by the differentiation of the DSL adsorption isotherm (eq 2), assuming constant loading ($dq = 0$) and substituting the result in the definition of isosteric heat equation (eq 4), resulting in the following equation[41,43,46]

$$(-\Delta H_{st}) = \frac{q_{m1}\frac{b_1 \Delta H_1}{(1+b_1 p)^2} + q_{m2}\frac{b_2 \Delta H_2}{(1+b_2 p)^2}}{q_{m1}\frac{b_1}{(1+b_1 p)^2} + q_{m2}\frac{b_2}{(1+b_2 p)^2}} \tag{6}$$

Selectivity and Working Capacity. The selectivity (α) of component i over component j can be defined as[47,48]

$$\alpha_{i,j} = \frac{q_i/q_j}{p_i/p_j} \tag{7}$$

where q_i and q_j are the adsorbed equilibrium concentration of components i and j at the same pressure and temperature, respectively. p_i and p_j are the respective partial pressures.

The working capacity of an adsorbent can be defined as the difference in the adsorption equilibrium concentration values between the high and low pressures in the case of PSA/VSA (at constant temperature) and from a high and low temperature in the case of TSA (at constant pressure). A general expression including both the temperature and pressure for the calculation of the working capacity is[49]

$$\beta_p = q(T_1, p_1) - q(T_2, p_2) \tag{8}$$

where $q(T_1, p_1)$ is the adsorbed equilibrium concentration at the temperature T_1 and partial pressure p_1 in the adsorption step and $q(T_2, p_2)$ is the adsorbed equilibrium concentration at temperature T_2 and regenerating pressure p_2 in the desorption step.

Breakthrough Mathematical Modeling. A mathematical model has been developed to predict the dynamic behavior of the fixed bed adsorption process for the single- and multicomponent breakthrough curves, which is described in

https://doi.org/10.1021/acs.iecr.1c02261
Ind. Eng. Chem. Res. 2021, 60, 15236−15247

Table 1. Adsorption Equilibrium Model Parameters for Sorption of CO_2, CH_4, and N_2 on Binder-Free Zeolite KY

	q_m (mol kg^{-1})		b (kPa^{-1})[a]		(ΔH_i) (kJ mol^{-1})		
species	q_{m1}	q_{m2}	b_1	b_2	$(\Delta H_i)_1$	$(\Delta H_i)_2$	R^2
CO_2	3.35	3.25	6.27×10^{-2}	1.62×10^{-1}	−45.0	−37.4	0.9990
CH_4	4.81		1.23×10^{-3}		−16.9		0.9994
N_2	2.98		8.30×10^{-4}		−18.7		0.9990

[a]The reference temperature used is 313 K.

Section S2 of the Supporting Information. Briefly, the mathematical model is based on the mass and energy conservation law principles including both the effect of the longitudinal axial dispersion of the flowing gas through the bed and an overall effective kinetic rate mechanism for mass transfer of the sorbates between the bulk gas phase and adsorbent particles (linear driving force model, LDF). The adsorption equilibrium isotherm is described by the DSL model. The resulting set of coupled partial and algebraic differential equations is summarized in Table S2, and the correlations used to estimate the mathematical model parameters are shown in Table S3.

RESULTS AND DISCUSSION

Adsorbent Properties and Characterization. N_2 gas sorption measurements were performed to describe the porous nature of the binder-free zeolite KY studied. The corresponding adsorption and desorption isotherms at 77 K are shown in Figure 1a. It can be seen that the isotherms are of type I according to the new IUPAC classification,[50] being concave to the p/p_0 axis with the loading reaching a limiting value, which is a signature characteristic of microporous materials. At the low-pressure region (between p/p_0 = 0.01 and 0.10), the adsorbed amount increases from approximately 150 to 200 cm^3_{STP}/g and then it practically remains constant until p/p_0 = 1. The textural properties of the material are summarized in Table S4.

The mercury (Hg) intrusion porosimetry outcomes are shown in Figure 1b, which are presented by differential intrusion/extrusion as a function of the pore size diameter. A pore size range is detected from nano- to micropore sizes (according to the new IUPAC scheme[50]) between 0.01 and 10 μm. The average pore size by extrusion is observed to be around 1 μm, indicating that most of the pores in the binder-free zeolite KY are considered to be between the size classes of sub- and intermicropores.

Scanning electron microscopy (SEM) images of the zeolite KY samples are presented in Figure 1c−g. Foggy crystals with an average size of around 1 μm with cubic/spherical characteristics can be observed in Figure 1f. However, in Figure 1g, it is possible to see the crystal intergrowth in the interior forming polycrystalline morphology, and a single zeolite crystal inside the beads is almost not perceptive. This behavior has already been observed[51] and was related to the manufacturing process of binder-free zeolite crystals.

Adsorption Equilibrium of CO_2, CH_4, and N_2 on Binder-Free Zeolite KY. The single-component adsorption equilibrium data of CO_2, CH_4, and N_2 on binder-free zeolite KY were collected at three temperatures, 313, 373, and 423 K, and for partial pressures up to 350 kPa directly from a series of fixed bed breakthrough experiments using eq 1. The experimental conditions for the single component breakthrough runs of CO_2, CH_4, and N_2 are summarized in Table S5. All the single-component breakthrough curves measured are depicted in Figures S2−S4.

Figure 2a1−c1 shows the isotherms collected for CO_2, CH_4, and N_2 as well as the fitting with the standard Langmuir (for CH_4 and N_2) and dual-site Langmuir (for CO_2) models, at (a1) 313, (b1) 373, and (c1) 423 K. As can be seen, the amount adsorbed of all components increases by enhancing the partial pressure and decreases by enhancing the temperature. At 313 K and 350 kPa, the adsorbed equilibrium concentrations for CO_2, CH_4, and N_2 in binder-free zeolite KY are around 6.42, 1.45, and 0.671 mol kg^{-1}, respectively. Regarding the CO_2 isotherms, it is clear that this guest molecule presents a much higher affinity with the binder-free zeolite KY than the other components, with this result being especially due to its large linear quadrupole moment and consequently strong interaction with the intracrystalline charge density framework.

Figure 2a2−c2 shows the numerical (eq 7) and experimental selectivities of CO_2 over N_2 (green) and CO_2 over CH_4 (blue) at the temperatures of (a2) 313, (b2) 373, and (c2) 423 K. At 313 K (Figure 2a2), it is visible that, at the interval of lower pressure from 5 to 10 kPa, the selectivity of CO_2 over N_2 is the highest ranging from 105 to 135. Under the same conditions, the selectivity of CO_2 over CH_4 is between 45 and 57. As the temperature increases, the selectivity of CO_2 over N_2 and CH_4 decreases as it does not exceed 29 and 10, respectively, at 423 K (Figure 2c2). At higher pressures from 150 to 350 kPa, the CO_2 selectivity over the other components generally becomes practically constant, as it is shown in Figure 2a2−c2. It is worth mentioning that, at the higher temperatures (373 and 423 K) and low pressures (below 50 kPa), CH_4 and N_2 concentration curves break through the column very fast (less than a minute), which can contribute to experimental errors in the measurement of the adsorption equilibrium experimental data (please see Figures S3 and S4 in the Supporting Information). Accordingly, this can lead to an under or over-measurement of the compounds adsorbed in equilibrium concentration, which results in the calculation of an unexpected lower experimental selectivity of CO_2 over N_2 and CH_4 at low pressure, as can be seen in Figure 2b2,c2.

Regarding the isotherm model fitting (lines in Figure 2a1−c1), the standard Langmuir model is reasonable to describe CH_4 and N_2 data because the adsorption binding sites in the surface can be considered practically homogeneous for the guest molecules. However, for the guest CO_2, the DSL isotherm model is more appropriate because the adsorbent surface can be considered energetically heterogeneous due to the different cation site locations.[35] Table 1 summarizes the DSL and Langmuir isotherm parameters for the adsorption of CO_2, CH_4, and N_2 in the binder-free zeolite KY as well as the respective fitting correlation coefficients. The extended dual-site Langmuir (DSL) model (eq 2) was used to fit the multicomponent data (binary and ternary adsorption equilibrium data), according to the approach presented by Ritter *et*

https://doi.org/10.1021/acs.iecr.1c02261
Ind. Eng. Chem. Res. 2021, 60, 15236−15247

al.[52] and Tynan *et al.*[53] (details are given in Section S6 in the Supporting Information). From the fitting procedure, the values calculated for q_{mi} follow the order CO_2(6.60 mol kg^{-1}) > CH_4(4.81 mol kg^{-1}) > N_2(2.98 mol kg^{-1}), giving rise to some thermodynamic inconsistency of the models. However, these values should be read as empirical values valid only for the proper description of experimental data by the simple DSL/Langmuir isotherm models in the range of temperature and pressure studied (extrapolation is not recommended). The same is true for the values of the adsorption affinity constant b_i reported in Table 1.

Figure 3 depicts the CO_2 isotherms at 313 K in the binder-free ion-exchanged KY and in the as-synthesized NaY form

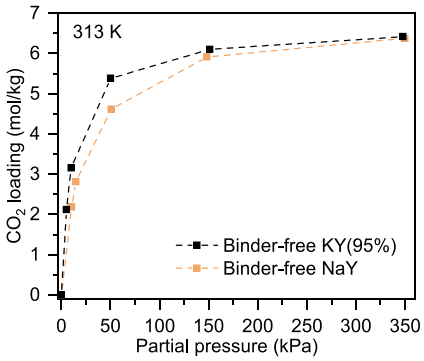

Figure 3. Comparison between the CO_2 adsorption equilibrium isotherm at 313 K and up to 350 kPa obtained in the binder-free ion-exchanged KY(95%) (black) with the one in the binder-free beads of NaY (light orange) from where the ion exchange is performed. Experimental = symbols.

(from where the ion exchange had been performed), for a comparison. As can be observed, the loading of CO_2 in the binder-free zeolite KY is higher up to 350 kPa. This result clearly indicates that the potassium ion exchange of Y zeolite enhances the amount adsorbed of CO_2 at low partial pressure, as already shown/predicted by other authors.[34,35] At 313 K and below 150 kPa, the difference in the loadings of CO_2 in the KY and NaY binder-free beads may reach up to 0.77 mol kg^{-1}, representing an increase of 16.6% in these conditions.

Figure S5a shows a comparison of the CO_2 isotherm data collected in this work with the ones in LiY(73%), KY(100%), and CsY(89%) zeolites in powder form prepared by ion exchange of a parent NaY sample with a Si/Al ratio of 2.5.[35] The results show that the adsorption capacity of the binder-free KY studied in this work is also very competitive compared to most of the studied alkali metal exchanged zeolites. At 150 kPa and 323 K, the adsorption equilibrium concentration of CO_2 in the binder-free KY is equal to 5.89 mol kg^{-1}, compared to 5.24 for NaY, 5.07 for KY, 4.45 for LiY, and 2.98 mol kg^{-1} for CsY (more details are provided in the Supporting Information Section S4). Another comparison with the powder form of KY zeolite is shown in Figure S5b for the CO_2 isotherms at 333 K,[35] which has a comparable ion exchange degree, in the pressure range until 100 kPa. As can be seen, the loading of CO_2 in the binder-free zeolite KY is systematically higher and follows a similar trend for this range of pressure.

The 13X zeolite reported by Hefti *et al.*[54] contains an adsorption inert binder (between 15 and 25%) that reduces its adsorption capacity. In this way, for the comparison of the 13X zeolite with the binder-free KY studied in this work, it was assumed that the 13X zeolite has a 15−25% higher capacity than the values reported by the authors. Accordingly, the amounts adsorbed of CO_2 at 15 kPa and 298 K in the binder-free zeolite KY are 9.3 and 0.5% higher than in 13X zeolite, respectively.

The isosteric heats of adsorption are calculated from the adsorption equilibrium data using eq 4 (details are shown in Figure S6 for all the compounds). Figure S7 shows the numerical predicted isosteric heat (eq 6) along with the calculated experimental values as a function of coverage, where the DSL model predicts the experimental observation of a practically constant net isosteric heat for CO_2, CH_4, and N_2 as a function of coverage with values around 39.9, 16.9, and 18.7 kJ mol^{-1}, respectively. The isosteric heat for N_2 is slightly higher than the one for CH_4, probably because it has also a quadrupole moment despite CH_4, which is an apolar molecule.

Binary Adsorption for Mixtures CO_2/N_2. Figure 4 shows the adsorption (a1−c1) and desorption (a2−c2) breakthrough curves for the mixture (CO_2/N_2:15/85) at 313, 373, and 423 K. The desorption step was performed with pure N_2 at the same flow rate used in the adsorption step. The experimental conditions for these set of runs can be found in Table S6 in the Supporting Information.

As can be seen in Figure 4a1, CO_2 starts to elute from the column at around 150 min with a mass transfer zone that reaches the inlet concentration (saturation of the bed) at around 250 min. The effect of temperature in the binary breakthrough curves CO_2/N_2 is shown in Figure 4a1−c1, where it can be observed that the saturation time decreases with increasing temperature as expected (313−423 K). Regarding the desorption curves with pure N_2 (Figure 4a2−c2), the time to clean the column is much higher than the time to saturate it, especially at 313 K (a2). This trend can be explained from the type I IUPAC classification of the isotherms, which are considered favorable for the adsorption and consequently unfavorable for desorption, resulting in a spreading of the mass transfer zone in the desorption step, which contributes to the longer time needed for the regeneration of the column. As the temperature increases from 313 to 423 K, the desorption time decreases from 1000 (numerical curve in Figure 4a2) to 40 min (Figure 4c2).

The working capacity for a TSA process, calculated between two different temperatures (313 and 423 K, eq 8) keeping the same feed conditions (CO_2/N_2:15/85 vol %) at constant 100 kPa, is equal to 3.7 mol kg^{-1}, which compares to 3.3 mol kg^{-1} observed in pellets of 13X zeolite[48] (we note that these pellets of 13X zeolite have an inert clay binder content that can reach up to 25% in weight according to Zeochem). Therefore, by using the binder-free zeolite KY, it is possible to achieve an increase in the working capacity for the TSA process up to 12.0%. The working capacity for a PSA process, calculated between two different partial pressures (15 and 3 kPa, eq 8) at a constant temperature of 298 K, is equal to 2.4 mol kg^{-1}, which compares to 1.3 mol kg^{-1} observed in pellets of 13X zeolite.[48] Therefore, by using the binder-free zeolite KY, it is possible to achieve an increase in working capacity for the PSA process up to 84.0%. These results show that the binder-free beads (ready to use for large-scale production) should be regarded as an important adsorbent material to be used to near atmospheric pressure for CO_2 capture for TSA or PSA processes. However, further comprehensive experimental investigation needs to be performed to confirm the effectiveness of the binder-free KY applied for the cyclic

https://doi.org/10.1021/acs.iecr.1c02261
Ind. Eng. Chem. Res. 2021, 60, 15236−15247

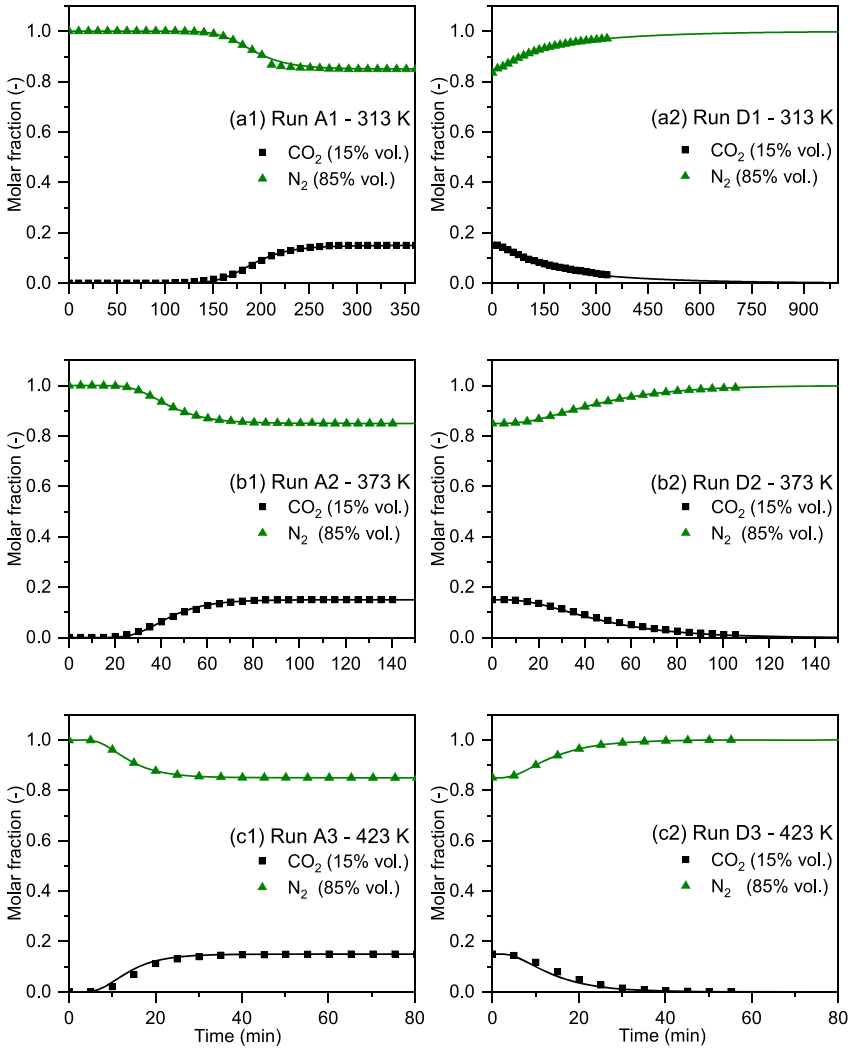

Figure 4. (a1, b1, c1) Adsorption (Run A) and (a2, b2, c2) desorption (Run D) breakthrough curves for CO_2 and N_2 on binder-free zeolite KY at 313, 373, and 423 K. Experimental = symbols; numerical = lines. Experimental conditions are summarized in Table S6 in the Supporting Information.

adsorption process for CO_2 post-combustion capture and biogas upgrading processes, but the results arising for this experimental study are very promising.

A comparison breakthrough study between experiments in the ion-exchanged binder-free KY and the as-synthesized NaY has been performed for the mixture CO_2/N_2 (15/85 vol %) at 313 K and a total pressure of 100 kPa. The result is illustrated in Figure S8a where it is clear that CO_2 elutes earlier in the fixed bed column with binder-free NaY, which means that CO_2 selectivity is higher in the KY form. This result is in accordance with the literature[34,35] predictions proving the advantage of using the potassium form to increase CO_2 selectivity compared to the NaY faujasite form, especially for CO_2 capture from post-combustion streams.

Additionally, Table S12 in the Supporting Information shows a comparison of the calculated values of binder-free KY metrics along with other adsorbents such as zeolite 13X, activated carbon (CS-AC), UTSA-16, and Mg-MOF-74, under post-combustion capture conditions shown in the literature.[48]

Ternary Adsorption of Mixtures $CO_2/CH_4/N_2$. Figure 5 shows breakthrough curves for ternary mixture feeds of $CO_2/CH_4/N_2$ (20/20/20 vol % balanced with He) on binder-free zeolite KY at 100 kPa and (a) 313, (b) 373, and (c) 423 K, under conditions typically used for biogas upgrading. As can be seen, the binder-free zeolite KY acts as an efficient separator of CO_2 from CH_4/N_2. CH_4 and N_2 practically elute from the column at the beginning of the experiments. Additionally, the ternary breakthrough curves exhibit the so-called roll-up phenomenon,[55] where the least adsorbed solutes (following the hierarchy order $N_2 < CH_4 \ll CO_2$) are desorbed by the more strongly adsorbed ones by an adsorption equilibrium competition displacement process. This phenomenon makes the concentration of the least adsorbed components (moving faster in the column: CH_4 and N_2) overcome the feed concentration until the strongest adsorbed component (moving slower in the column: CO_2) starts to elute the column, as is clearly shown in Figure 5.

Table S7 in the Supporting Information shows the experimental conditions for the runs involving the ternary mixture.

Similar to the binary experiments, values of the adsorption capacity, selectivity, and working capacity were determined for the experiments at 100 kPa. At 313 K, the selectivities of CO_2 over CH_4 are around 19 and 45 over N_2. The working capacity was predicted between 313 and 423 K while keeping the same feed conditions, where the value is equal to 4.0 mol kg^{-1}.

https://doi.org/10.1021/acs.iecr.1c02261
Ind. Eng. Chem. Res. 2021, 60, 15236−15247

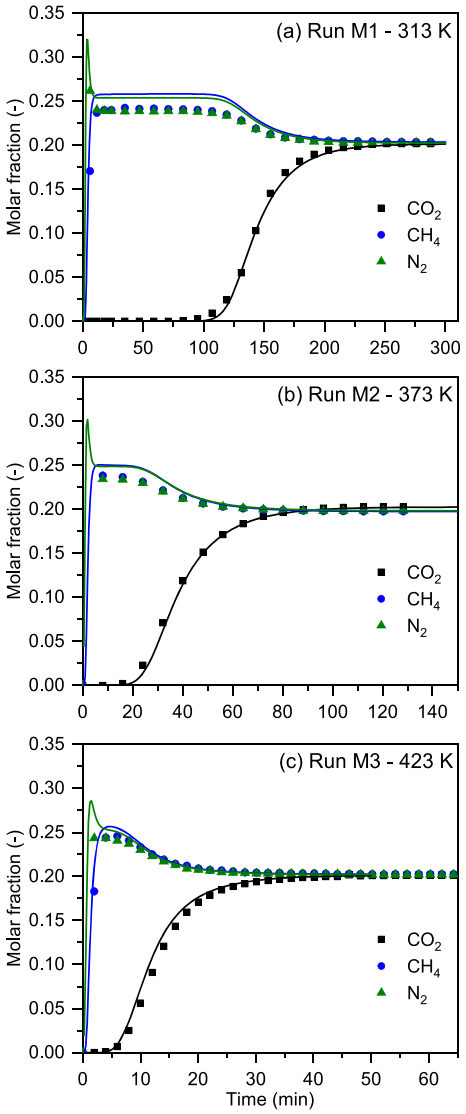

Figure 5. Ternary adsorption breakthrough curves for $CO_2/CH_4/N_2$ on binder-free zeolite KY at (a) 313, (b) 373, and (c) 423 K. Experimental = symbols; numerical = lines. Experimental conditions are summarized in Table S7 in the Supporting Information.

These results indicate also an efficient separation of CO_2 from the $CO_2/CH_4/N_2$ ternary mixture.

Also, a comparison study between breakthrough experiments in the ion-exchanged binder-free KY and the as-synthesized NaY has been performed for the mixture $CO_2/CH_4/N_2$ (20/20/20 vol % balanced with He) at 313 K and 100 kPa. Once more, in Figure S8b, it is possible to observe that CO_2 breaks through the column earlier in the bed containing binder-free NaY, proving once more the advantage of using the potassium form to increase CO_2 selectivity, also under biogas upgrading conditions.

To verify the lifetime/recyclability of the binder-free zeolite KY, at the end of the single and multicomponent experiments, five CO_2 breakthrough experiments were repeated at the experimental conditions of RUN 1.3 (50 kPa and 313 K). After each run, the material was cleaned at 473 K with a pure He stream (80 mL min^{-1}) for at least 2 h. Table S14 summarizes the experimental conditions for these runs. Figure S9a illustrates the CO_2 breakthrough curves plotted in terms of the normalized molar fraction (y_i/y_{i0}) as a function of moles fed per unit mass of the adsorbent, and Figure S9b shows the loadings of CO_2 calculated for each run. It can be observed that the calculated CO_2 loadings for all runs are almost identical (c.a. 5.37 mol kg^{-1}), which confirms that the material can be regenerated and reused several times without capacity lost.

Modeling of Binary and Ternary Breakthrough Data $CO_2/CH_4/N_2$. The modeling of breakthrough curves is important to understand physically the overall fixed bed adsorption experimental dynamics for thereafter design cyclic adsorption processes. Accordingly, the fixed bed adsorption model (shown in Table S2 in the Supporting Information) was used to simulate/predict the binary and ternary breakthrough experimental data.[41,56]

The spreading of mass transfer zones in a fixed bed is influenced mainly by (i) the nature of adsorption equilibrium (favorable or unfavorable), (ii) mass transfer of sorbates between the bulk gas phase and the interior of the porous particles, and (iii) the flow pattern of the gas in the fixed bed, which can be characterized by an axial dispersion model. Accordingly, it is important to evaluate the relative importance of each type of mechanism on the overall dynamics and respective influence in the spreading of mass transfer zones of the breakthrough curves.

Concerning the adsorption equilibrium, the isotherms are all type I (favorable for adsorption), so their effect is to narrow the length of the mass transfer zone. The mass transfer kinetics mechanism analysis of the adsorbable species from the bulk gas phase to the interior of the adsorbent can be very complex, but generally, it can be simplified by the so-called linear driving force model (LDF).[57,58] In this approach, a lumped parameter called the overall mass transfer coefficient, K_{LDF}, can be related to the several possible resistances to mass transfer in a bidisperse porous adsorbent such as film diffusion, macropore diffusion, and micropore diffusion, linked by the following equation, which takes into account the relative importance of each mechanism based on the respective time constants

$$\frac{1}{K_{LDF}} = \frac{R_p}{3k_f} + \frac{R_p^2}{15\varepsilon_p D_p} + \frac{r_c^2}{15KD_c} \tag{9}$$

where K is the dimensionless Henry's law equilibrium constant, R_p is the particle (bead) radius, ε_p is the particle porosity, D_p is the effective macropore diffusivity, r_c is the zeolite crystal radius (from where the beads were made), and D_c is the intracrystalline/framework zeolite diffusivity.

Ruthven[31] used the method of moments for a linear system to evaluate also the relative importance of the axial dispersion of the gas flowing through the bed relatively to the mass-transfer resistances (eq 9) providing an overall effective rate coefficient k', given by the following equation

$$\frac{1}{k'K} = \frac{D_{ax}}{v_i^2}\left(\frac{1-\varepsilon_b}{\varepsilon_b}\right) + \frac{R_p}{3k_f} + \frac{R_p^2}{15\varepsilon_p D_p} + \frac{r_c^2}{15KD_c} \tag{10}$$

where k' is the overall effective rate coefficient, D_{ax} is the axial dispersion of the gas in the bed, v_i is the interstitial velocity, and ε_b is the bed porosity.

By comparing the relative values of the time constants of each mechanism (terms of the r.h.s. in eq 10), it is possible to evaluate roughly which is the relevant one that influences the spreading of the mass transfer zones of the breakthrough curves. Table S3 in the Supporting Information summarizes

https://doi.org/10.1021/acs.iecr.1c02261
Ind. Eng. Chem. Res. 2021, 60, 15236−15247

the correlations used to predict the values of each parameter of the l.h.s. of eq 9 and r.h.s. of eq 10, and Tables S8 and S9 in the Supporting Information summarize the values calculated for each term of eqs 9 and 10 for the binary (CO_2/N_2) and ternary ($CO_2/CH_4/N_2$) experiments at 313, 373, and 423 K, respectively. For the binary experiments (Table S8), we can read that the values of the term related to axial dispersion vary from 1.81 to 2.75 s being much higher than the reverse of the overall mass-transfer coefficient K_{LDF}, which varies from 0.04 to 0.06 s, indicating that the axial dispersion of the flowing gas through the bed will have a significant influence on the length of the mass transfer zones of the experimental breakthrough curves studied in this work. Similarly, for the ternary experiments, the same behavior is observed (Table S9). This is demonstrated in Figure 6a where a selected binary

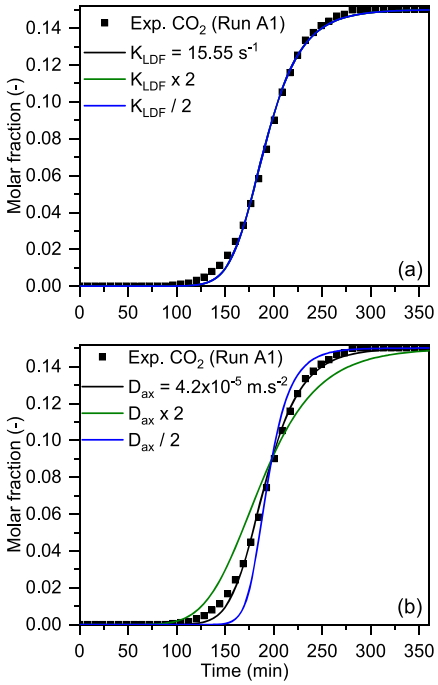

Figure 6. Influence of changing overall mass transfer coefficient K_{LDF} (a) and axial dispersion D_{ax} (b) on the numerical breakthrough curves of CO_2 at 313 K and 0.15 bar partial pressure balanced with N_2 (Run A1, see Tables S6 and S8 in the Supporting Information for experimental conditions and model parameters, respectively). Experimental = symbols; numerical = lines.

experiment (Run A1) is simulated by changing the values of the overall mass-transfer coefficient (K_{LDF}) for a fixed value of D_{ax}. It can be observed in Figure 6a that there is no effect in the spreading of the breakthrough curves. On the contrary, Figure 6b shows that the spread of the mass transfer zone of the breakthrough curves is strongly affected by changing the values of the axial dispersion (D_{ax}) for a constant value of K_{LDF}. This parametric study clearly shows that the spreading of the breakthrough curves is completely dominated by the axial dispersion, a result confirmed by the values of each term of eq 10, as shown in Tables S8 and S9 in the Supporting Information.

Overall, the numerical simulations (lines in Figures 4 and 5) describe with good accuracy the dynamics of the fixed bed adsorption system for both the adsorption and desorption steps, in binary and ternary experiments, being the mathematical model that developed a valuable tool for the design and prediction of the cyclic operation of industrial processes (PSA and TSA) using binder-free zeolite beads of KY for post-combustion and biogas upgrading processes.

Finally, we should remark that the previously described methodology for calculating model parameters to be used as a predictive tool is based on the assumption that the interior of the binder-free beads is made with very well-identified single crystals (as in typical commercial binder pellets/beads) with a size of around 1 μm from where they were synthesized and also on framework/crystal diffusivities (D_c) calculated from molecular dynamics simulations (MDS) and the experimental quasi-elastic neutron scattering (QENS) technique[59,60] (a microscopic experimental technique where the values of D_c are generally much higher than the ones measured by the macroscopic ones[61]). Accordingly, very small values for the micropore diffusion time constant term $r_c^2/(15KD_c)$ in eqs 9 and 10 (values given in Tables S8 and S9 in the Supporting Information) are obtained, and consequently, the micropore diffusion resistance mechanism effect is negligible for the value of the global mass transfer coefficient. However, the manufacture of mechanically stable binder-free beads is a complex process,[51] where in the end, the interior of the binder-free beads is made of random-sized polycrystals, as can be observed in the SEM photographs shown in Figure 1f. Accordingly, in practice, the value of the crystal size (r_c) to be used in eqs 9 and 10 is indeed very difficult to select. This means also that, in eqs 9 and 10, we should correctly write an average $\langle r_c \rangle$ for the polycrystals observed in Figure 1f, where the true value is unknown, and the value of D_c could be also different from the one measured by MDS, QENS, or even NMR. This particularity can significantly affect the relative importance of micropore versus macropore diffusion in these bidisperse binder-free adsorbents, or we can assume that we have an unknown rate mechanism in the binder-free beads[62] due to the presence of polycrystals. However, for the present system studied, since the gas flow through the fixed bed is very small, we believe that the system is with no doubt dominated by the effect of the longitudinal degree of backmixing of the gas flow pattern through the fixed bed quantified by the axial dispersion coefficient (D_{ax}) from where the respective time constant term and respective value in eq 10 (ranging from 1.81 to 2.75 s) superimpose largely to the importance of the global mass transfer coefficient (K_{LDF}) (values ranging from 0.04 to 0.06 s), as demonstrated in Tables S8 and S9, and globally shown by the goodness of the fits of the simulated breakthrough curves presented in Figures 4 and 5.

CONCLUSIONS

This work presents a systematic study of new potassium-exchanged binder-free beads of Y zeolite for the fixed bed adsorption of CO_2, CH_4, and N_2 and their mixtures, with interest for CO_2 post-combustion capture and biogas upgrading strategies. It was demonstrated experimentally, from binary/ternary breakthrough curves, that this new binder-free zeolite KY (ready to be used and scaled up for large production) separates with a very high selectivity CO_2 from mixtures containing $CO_2/CH_4/N_2$ and enhances the CO_2 adsorption uptake at 15 kPa up to 10% regarding commercial 13X (NaX) zeolite beads in the presence of N_2. The selectivity of CO_2 over N_2, from post-combustion streams conditions, is around 104 at 298 K, and the selectivities of CO_2 over CH_4 and N_2 in the ternary system are around 14 and 32 at

https://doi.org/10.1021/acs.iecr.1c02261
Ind. Eng. Chem. Res. 2021, 60, 15236−15247

313 K, respectively. The experimental data have been modeled through a suitable mathematical model that provides a good description of the overall breakthrough data, being a useful tool for the design of cyclic adsorption processes using the new binder-free beads.

■ ASSOCIATED CONTENT

Supporting Information

The Supporting Information is available free of charge at https://pubs.acs.org/doi/10.1021/acs.iecr.1c02261.

Effect of zeolite structural characteristics and ion exchange on CO_2 adsorption; mathematical modeling of single- and multicomponent fixed bed breakthrough curves; conversion from molecules/UC into mol kg^{-1}; comparison of CO_2 adsorption equilibrium data in different ion-exchanged zeolites; comparison of adsorbent metrics with different zeolites under flue gas conditions; experimental conditions for single, binary, and ternary experiments; and multicomponent equilibria prediction (PDF)

■ AUTHOR INFORMATION

Corresponding Authors

Lucas F.A.S. Zafanelli − *Centro de Investigação de Montanha (CIMO), Instituto Politécnico de Bragança, 5300-253 Bragança, Portugal; Laboratory of Separation and Reaction Engineering (LSRE), Associate Laboratory LSRE/LCM, Department of Chemical Engineering, Faculty of Engineering, University of Porto, 4099-002 Porto, Portugal;* orcid.org/0000-0001-5187-2042; Email: zafanelli@ipb.pt

José A.C. Silva − *Centro de Investigação de Montanha (CIMO), Instituto Politécnico de Bragança, 5300-253 Bragança, Portugal;* orcid.org/0000-0003-1778-3833; Email: jsilva@ipb.pt

Authors

Ezzeldin Aly − *Centro de Investigação de Montanha (CIMO), Instituto Politécnico de Bragança, 5300-253 Bragança, Portugal;* orcid.org/0000-0003-4840-2597

Adriano Henrique − *Centro de Investigação de Montanha (CIMO), Instituto Politécnico de Bragança, 5300-253 Bragança, Portugal; Laboratory of Separation and Reaction Engineering (LSRE), Associate Laboratory LSRE/LCM, Department of Chemical Engineering, Faculty of Engineering, University of Porto, 4099-002 Porto, Portugal;* orcid.org/0000-0002-5227-9790

Marcella Golini Pires − *Centro de Investigação de Montanha (CIMO), Instituto Politécnico de Bragança, 5300-253 Bragança, Portugal*

Alírio E. Rodrigues − *Laboratory of Separation and Reaction Engineering (LSRE), Associate Laboratory LSRE/LCM, Department of Chemical Engineering, Faculty of Engineering, University of Porto, 4099-002 Porto, Portugal;* orcid.org/0000-0002-0715-4761

Kristin Gleichmann − *Chemiewerk Bad Köstritz GmbH, 07586 Bad Köstritz, Germany*

Complete contact information is available at: https://pubs.acs.org/10.1021/acs.iecr.1c02261

Notes

The authors declare no competing financial interest.

■ ACKNOWLEDGMENTS

The authors thank the Foundation for Science and Technology (FCT, Portugal) and ERDF under Programme PT2020 to CIMO (UID/AGR/00690/2019) and POCI-01-0145-FEDER006984-Associate Laboratory LSRE-LCM. The authors also thank the Foundation for Science and Technology (FCT, Portugal) under Programme PTDC 2020 * 3599-PPCDTI * Engenharia dos Processos Químicos * project PTDC/EQU-EPQ/0467/2020. Last, the authors thank the Foundation for Science and Technology (FCT, Portugal) through the individual research grants SFRH/BD/148525/2019 for A.H. and DFA/BD/7925/2020 for L.F.A.S.Z.

■ NOMENCLATURE

a_p	specific area of the pellet (m^{-1})
a_c	specific area of the column (m^{-1})
b_i	adsorption equilibrium affinity constant of component i (Pa^{-1})
b_∞	pre-exponential factor of the affinity constant (Pa^{-1})
C	total gas concentration (mol m^{-3})
C_{0i}	feed gas-phase concentration at the inlet of the fixed bed (mol m^{-3})
C_{pg}	heat capacity of gas (J mol^{-1} K^{-1})
C_{ps}	heat capacity of the adsorbent (J mol^{-1} K^{-1})
d_p	bead diameter (m)
d_c	column diameter (m)
D_{ax}	axial mass dispersion coefficient (m^2 s^{-1})
D_c	intracrystalline diffusivity (m^2 s^{-1})
D_k	Knudsen diffusivity (m^2 s^{-1})
D_m	molecular diffusivity (m^2 s^{-1})
D_p	effective macropore diffusivity (m^2 s^{-1})
$F_{f,i}$	feed molar flow rate of component i at the inlet of the bed (mol m^{-2} s^{-1})
F_i	feed molar flow rate of component i at the outlet of the bed (mol m^{-2} s^{-1})
h_p	film heat transfer coefficient (W m^{-2} K^{-1})
h_w	wall heat transfer coefficient (W m^{-2} K^{-1})
k'	overall effective rate coefficient (s^{-1})
K	dimensionless Henry's law equilibrium constant (−)
K_{LDF}	linear driving force coefficient (s^{-1})
K_{ax}	effective axial bed thermal conductivity (W m^{-1} K^{-1})
L	length of the column (m)
Nu	Nusselt number
p_i	partial pressure of component i (Pa)
P	total pressure of the column (Pa)
Pe	Peclet number
q_i	adsorption concentration of component i (mol kg^{-1})
$\overline{q}_i$	average adsorption concentration of component i (mol kg^{-1})
q_{cal}	calculated adsorption concentration (mol kg^{-1})
$\overline{q}_{cal}$	average adsorption concentration (mol kg^{-1})
q_m	maximum adsorption equilibrium concentration (mol kg^{-1})
r_p	pore radius (Å)
r_c	crystal radius (m)
R_p	pellet radius (m)
R	universal gas constant (J mol^{-1} K^{-1})
Re	Reynolds number
S_{BET}	BET surface area (m^2 g^{-1})
S_{ext}	external surface area (m^2 g^{-1})
$S_{Langmuir}$	Langmuir surface area (m^2 g^{-1})
S_{mic}	micropore surface area (m^2 g^{-1})

t	time (s)
t_n	saturation time (s)
T	temperature in the bulk gas phase (K)
T_s	temperature in the solid phase (K)
T_w	column wall temperature (K)
v	superficial velocity (m s^{-1})
v_i	interstitial velocity (m s^{-1})
V_c	column volume (m^3)
V_{mic}	micropore volume (mm^3 g^{-1})
V_{Total}	total pore volume (mm^3 g^{-1})
V_{mic}	average pore width (nm)
y_i	molar fraction of sorbate species i in the bulk phase
y_{i0}	feed molar fraction of sorbate species i in the bulk phase
z	axial coordinate in bed (m)

GREEK LETTERS

α_P	pure component selectivity (-)
α_C	competitive component selectivity (-)
β_P	pure working capacity (mol kg^{-1})
β_C	competitive working capacity (mol kg^{-1})
ΔH_i	isosteric heat adsorption of species i (J mol^{-1})
ε_b	bed porosity
ε_p	solid porosity
ρ_s	apparent adsorbent density (kg m^{-3})
τ	tortuosity
θ	$=q/q_m$

REFERENCES

(1) Gabrielli, P.; Gazzani, M.; Mazzotti, M. The Role of Carbon Capture and Utilization, Carbon Capture and Storage, and Biomass to Enable a Net-Zero-CO_2 Emissions Chemical Industry. *Ind. Eng. Chem. Res.* **2020**, *59*, 7033−7045.

(2) Jiménez, V.; Ramírez-Lucas, A.; Díaz, J. A.; Sánchez, P.; Romero, A. CO_2 Capture in Different Carbon Materials. *Environ. Sci. Technol.* **2012**, *46*, 7407−7414.

(3) D'Alessandro, D. M.; Smit, B.; Long, J. R. Carbon Dioxide Capture: Prospects for New Materials. *Angew. Chem. Int. Ed.* **2010**, *49*, 6058−6082.

(4) Stuckert, N. R.; Yang, R. T. CO_2 Capture from the Atmosphere and Simultaneous Concentration Using Zeolites and Amine-Grafted SBA-15. *Environ. Sci. Technol.* **2011**, *45*, 10257−10264.

(5) Zhao, Y.; Shen, Y.; Ma, G.; Hao, R. Adsorption Separation of Carbon Dioxide from Flue Gas by a Molecularly Imprinted Adsorbent. *Environ. Sci. Technol.* **2014**, *48*, 1601−1608.

(6) Yucel, H.; Ruthven, D. M. Diffusion in 5A Zeolite. Study of the Effect of Crystal Size. *J. Chem. Soc. Faraday Trans. 1 Phys. Chem. Condens. Phases* **1980**, *76*, 71.

(7) Espinal, L.; Poster, D. L.; Wong-Ng, W.; Allen, A. J.; Green, M. L. Measurement, Standards, and Data Needs for CO_2 Capture Materials: A Critical Review. *Environ. Sci. Technol.* **2013**, *47*, 11960−11975.

(8) Bui, M.; Adjiman, C. S.; Bardow, A.; Anthony, E. J.; Boston, A.; Brown, S.; Fennell, P. S.; Fuss, S.; Galindo, A.; Hackett, L. A.; Hallett, J. P.; Herzog, H. J.; Jackson, G.; Kemper, J.; Krevor, S.; Maitland, G. C.; Matuszewski, M.; Metcalfe, I. S.; Petit, C.; Puxty, G.; Reimer, J.; Reiner, D. M.; Rubin, E. S.; Scott, S. A.; Shah, N.; Smit, B.; Trusler, J. P. M.; Webley, P.; Wilcox, J.; Mac Dowell, N. Carbon Capture and Storage (CCS): The Way Forward. *Energy Environ. Sci.* **2018**, *11*, 1062−1176.

(9) Al-Mamoori, A.; Krishnamurthy, A.; Rownaghi, A. A.; Rezaei, F. Carbon Capture and Utilization Update. *Energy Technol.* **2017**, *5*, 834−849.

(10) Xiao, G.; Xiao, P.; Hoadley, A.; Webley, P. Integrated Adsorption and Absorption Process for Post-Combustion CO_2 Capture. *Front. Chem. Sci. Eng.* **2021**, *15*, 483−492.

(11) Wang, M.; Lawal, A.; Stephenson, P.; Sidders, J.; Ramshaw, C. Post-Combustion CO_2 Capture with Chemical Absorption: A State-of-the-Art Review. *Chem. Eng. Res. Des.* **2011**, *89*, 1609−1624.

(12) Dantas, T. L.; Rodrigues, A. E.; Moreira, R. F. P. M. Separation of Carbon Dioxide from Flue Gas Using Adsorption on Porous Solids. In *Greenhouse Gases - Capturing, Utilization and Reduction*; InTech: 2012, DOI: 10.5772/31917.

(13) Jiang, K.; Feron, P.; Cousins, A.; Zhai, R.; Li, K. Achieving Zero/Negative-Emissions Coal-Fired Power Plants Using Amine-Based Postcombustion CO_2 Capture Technology and Biomass Cocombustion. *Environ. Sci. Technol.* **2020**, *54*, 2429−2438.

(14) Lee, S.-Y.; Park, S.-J. A Review on Solid Adsorbents for Carbon Dioxide Capture. *J. Ind. Eng. Chem.* **2015**, *23*, 1−11.

(15) Bhown, A. S.; Freeman, B. C. Analysis and Status of Post-Combustion Carbon Dioxide Capture Technologies. *Environ. Sci. Technol.* **2011**, *45*, 8624−8632.

(16) Sircar, S. Separation of Methane and Carbon Dioxide Gas Mixtures by Pressure Swing Adsorption. *Sep. Sci. Technol.* **1988**, *23*, 519−529.

(17) Bari, S. Effect of Carbon Dioxide on the Performance of Biogas/Diesel Duel-Fuel Engine. *Renewable Energy* **1996**, *9*, 1007−1010.

(18) Yousef, A. M. I.; Eldrainy, Y. A.; El-Maghlany, W. M.; Attia, A. Upgrading Biogas by a Low-Temperature CO_2 Removal Technique. *Alexandria Eng. J.* **2016**, *55*, 1143−1150.

(19) Ghoufi, A.; Gaberova, L.; Rouquerol, J.; Vincent, D.; Llewellyn, P. L.; Maurin, G. Adsorption of CO_2, CH_4 and Their Binary Mixture in Faujasite NaY: A Combination of Molecular Simulations with Gravimetry−Manometry and Microcalorimetry Measurements. *Microporous Mesoporous Mater.* **2009**, *119*, 117−128.

(20) Shen, X.; Yan, F.; Li, C.; Qu, F.; Wang, Y.; Zhang, Z. Biogas Upgrading via Cyclic CO_2 Adsorption: Application of Highly Regenerable PEI@nano-Al_2O_3 Adsorbents with Anti-Urea Properties. *Environ. Sci. Technol.* **2021**, *55*, 5236−5247.

(21) Cavenati, S.; Grande, C. A.; Rodrigues, A. E. Layered Pressure Swing Adsorption for Methane Recovery from $CH_4/CO_2/N_2$ Streams. *Adsorption* **2005**, *11*, 549−554.

(22) Mulgundmath, V. P.; Tezel, F. H.; Saatcioglu, T.; Golden, T. C. Adsorption and Separation of CO_2/N_2 and CO_2/CH_4 by 13X Zeolite. *Can. J. Chem. Eng.* **2012**, *90*, 730−738.

(23) Sun, Q.; Li, H.; Yan, J.; Liu, L.; Yu, Z.; Yu, X. Selection of Appropriate Biogas Upgrading Technology-a Review of Biogas Cleaning, Upgrading and Utilisation. *Renewable Sustainable Energy Rev.* **2015**, *51*, 521−532.

(24) Silva, J. A. C.; Schumann, K.; Rodrigues, A. E. Sorption and Kinetics of CO_2 and CH_4 in Binderless Beads of 13X Zeolite. *Microporous Mesoporous Mater.* **2012**, *158*, 219−228.

(25) Silva, J. A. C.; Ferreira, A.; Mendes, P. A. P.; Cunha, A. F.; Gleichmann, K.; Rodrigues, A. E. Adsorption Equilibrium and Dynamics of Fixed Bed Adsorption of CH_4/N_2 in Binderless Beads of 5A Zeolite. *Ind. Eng. Chem. Res.* **2015**, *54*, 6390−6399.

(26) Silva, J. A. C.; Cunha, A. F.; Schumann, K.; Rodrigues, A. E. Binary Adsorption of CO_2/CH_4 in Binderless Beads of 13X Zeolite. *Microporous Mesoporous Mater.* **2014**, *187*, 100−107.

(27) Burns, T. D.; Pai, K. N.; Subraveti, S. G.; Collins, S. P.; Krykunov, M.; Rajendran, A.; Woo, T. K. Prediction of MOF Performance in Vacuum Swing Adsorption Systems for Postcombustion CO_2 Capture Based on Integrated Molecular Simulations, Process Optimizations, and Machine Learning Models. *Environ. Sci. Technol.* **2020**, *54*, 4536−4544.

(28) Mohr, R. J.; Vorkapic, D.; Rao, M. B.; Sircar, S. Pure and Binary Gas Adsorption Equilibria and Kinetics of Methane and Nitrogen on 4A Zeolite by Isotope Exchange Technique. *Adsorption* **1999**, *5*, 145−158.

(29) Ahn, H.; Moon, J. H.; Hyun, S. H.; Lee, C. H. Diffusion Mechanism of Carbon Dioxide in Zeolite 4A and CaX Pellets. *Adsorption* **2004**, *10*, 111−128.

(30) Seabra, R.; Ribeiro, A. M.; Gleichmann, K.; Ferreira, A. F. P.; Rodrigues, A. E. Adsorption Equilibrium and Kinetics of Carbon

https://doi.org/10.1021/acs.iecr.1c02261
Ind. Eng. Chem. Res. 2021, 60, 15236−15247

Dioxide, Methane and Nitrogen on Binderless Zeolite 4A Adsorbents. *Microporous Mesoporous Mater.* **2019**, *277*, 105−114.
(31) Ruthven, D. M. *Principles of Adsorption and Adsorption Processes*; 1st ed.; John Wiley & Sons: New York, 1984.
(32) Stamires, D. N. Properties of the Zeolite, Faujasite, Substitutional Series: A Review with New Data. *Clays Clay Miner.* **1973**, *21*, 379−389.
(33) Barrer, R. M.; Gibbons, R. M. Zeolitic Carbon Dioxide: Energetics and Equilibria in Relation to Exchangeable Cations in Faujasite. *Trans. Faraday Soc.* **1965**, *61*, 948.
(34) Walton, K. S.; Abney, M. B.; Douglas LeVan, M. CO_2 Adsorption in Y and X Zeolites Modified by Alkali Metal Cation Exchange. *Microporous Mesoporous Mater.* **2006**, *91*, 78−84.
(35) Pirngruber, G. D.; Raybaud, P.; Belmabkhout, Y.; Čejka, J.; Zukal, A. The Role of the Extra-Framework Cations in the Adsorption of CO_2 on Faujasite Y. *Phys. Chem. Chem. Phys.* **2010**, *12*, 13534.
(36) Bonenfant, D.; Kharoune, M.; Niquette, P.; Mimeault, M.; Hausler, R. Advances in Principal Factors Influencing Carbon Dioxide Adsorption on Zeolites. *Sci. Technol. Adv. Mater.* **2008**, *9*, No. 013007.
(37) Khvoshchev, S. S.; Zverev, A. V. Calorimetric Study of NH_3 and CO_2 Adsorption on Synthetic Faujasites with Ca^{2+}, Mg^{2+}, and La^{3+} Cations. *J. Colloid Interface Sci.* **1991**, *144*, 571−578.
(38) Shah, D. B.; Ruthven, D. M. Measurement of Zeolitic Diffusivities and Equilibrium Isotherms by Chromatography. *AIChE J.* **1977**, *23*, 804−809.
(39) Ruthven, D. M.; Kumar, R. A Chromatographic Study of the Diffusion of N_2, CH_4 and Binary CH_4-N_2 Mixtures in 4A Molecular Sieve. *Can. J. Chem. Eng.* **1979**, *57*, 342−348.
(40) Gleichmann, K.; Unger, B.; Brandt, A. Industrial Zeolite Molecular Sieves. In *Intech*; 2016; Vol. *i*, p 13.
(41) Zafanelli, L. F. A. S.; Henrique, A.; Karimi, M.; Rodrigues, A. E.; Silva, J. A. C. Single- and Multicomponent Fixed Bed Adsorption of CO_2, CH_4, and N_2 in Binder-Free Beads of 4A Zeolite. *Ind. Eng. Chem. Res.* **2020**, *59*, 13724−13734.
(42) Schumann, K.; Brandt, A.; Unger, B.; Scheffler, F. Bindemittelfreie Zeolithische Molekularsiebe Der Typen LTA Und FAU. *Chem. Ing. Tech.* **2011**, *83*, 2237−2243.
(43) Do, D. D. Series on Chemical Engineering. *Adsorption Analysis: Equilibria and Kinetics*; Imperial College Press, 1998, Vol. *2*.
(44) Hammed, B. H.; Foo, K. Y. Insights into the Modeling of Adsorption Isotherm Systems. *Elsevier* **2010**, *8*, 2−10.
(45) Barrer, R. M. *Zeolites and Clay Minerals as Sorbents and Molecular Sieves, VII*; Academic Press: London, 1978.
(46) Henrique, A.; Karimi, M.; Silva, J. A. C.; Rodrigues, A. E. Analyses of Adsorption Behavior of CO_2, CH_4, and N_2 on Different Types of BETA Zeolites. *Chem. Eng. Technol.* **2019**, *42*, 327−342.
(47) Harlick, P. J. E.; Tezel, F. H. An Experimental Adsorbent Screening Study for CO_2 Removal from N_2. *Microporous Mesoporous Mater.* **2004**, *76*, 71−79.
(48) Rajagopalan, A. K.; Avila, A. M.; Rajendran, A. Do Adsorbent Screening Metrics Predict Process Performance? A Process Optimisation Based Study for Post-Combustion Capture of CO_2. *Int. J. Greenhouse. Gas Control* **2016**, *46*, 76−85.
(49) Zhao, Q.; Wu, F.; Men, Y.; Fang, X.; Zhao, J.; Xiao, P.; Webley, P. A.; Grande, C. A. CO_2 Capture Using a Novel Hybrid Monolith (H-ZSM5/Activated Carbon) as Adsorbent by Combined Vacuum and Electric Swing Adsorption (VESA). *Chem. Eng. J.* **2019**, *358*, 707−717.
(50) Mays, T. J. A New Classification of Pore Sizes. In *Studies in Surface Science and Catalysis*; Elsevier Inc., 2007; Vol. *160*, pp. 57−62.
(51) Schumann, K.; Unger, B.; Brandt, A.; Scheffler, F. Investigation on the Pore Structure of Binderless Zeolite 13× Shapes. *Microporous Mesoporous Mater.* **2012**, *154*, 119−123.
(52) Ritter, J. A.; Bumiller, K. C.; Tynan, K. J.; Ebner, A. D. On the Use of the Dual Process Langmuir Model for Binary Gas Mixture Components That Exhibit Single Process or Linear Isotherms. *Adsorption* **2019**, *25*, 1511−1523.
(53) Tynan, K. J.; Tosso, S.; Ebner, A. D.; Ritter, J. A. On the Use of Single, Dual and Three Process Langmuir Models for Binary Gas Mixtures That Exhibit Unique Combinations of These Processes. *Adsorption* **2021**, *27*, 637−658.
(54) Hefti, M.; Marx, D.; Joss, L.; Mazzotti, M. Adsorption Equilibrium of Binary Mixtures of Carbon Dioxide and Nitrogen on Zeolites ZSM-5 and 13X. *Microporous Mesoporous Mater.* **2015**, *215*, 215−228.
(55) Helfferich, F.; Klein, G. *Multicomponent Chromatography: Theory of Interference. Marcel Dekker New York, USA* 1970.
(56) Henrique, A.; Rodrigues, A. E.; Silva, J. A. C. Separation of Hexane Isomers in ZIF-8 by Fixed Bed Adsorption. *Ind. Eng. Chem. Res.* **2019**, *58*, 378−394.
(57) Glueckauf, E. Theory of Chromatography. *J. Chromatogr. Libr.* **1955**, *51*, A1−A68.
(58) Streb, A.; Mazzotti, M. Adsorption for Efficient Low Carbon Hydrogen Production: Part 1—Adsorption Equilibrium and Breakthrough Studies for $H_2/CO_2/CH_4$ on Zeolite 13X. *Adsorption* **2021**, *27*, 541−558.
(59) Déroche, I.; Maurin, G.; Borah, B. J.; Yashonath, S.; Jobic, H. Diffusion of Pure CH_4 and Its Binary Mixture with CO_2 in Faujasite NaY: A Combination of Neutron Scattering Experiments and Molecular Dynamics Simulations. *J. Phys. Chem. C* **2010**, *114*, 5027−5034.
(60) Plant, D.; Jobic, H.; Llewellyn, P.; Maurin, G. CO_2 Diffusivity in LiY and NaY Faujasite Systems: A Combination of Molecular Dynamics Simulations and Quasi-Elastic Neutron Scattering Experiments. *Adsorption* **2007**, *13*, 209−214.
(61) Onyestyák, G.; Rees, L. V. C. Frequency Response Study of Adsorbate Mobilities of Different Character in Various Commercial Adsorbents. *J. Phys. Chem. B* **1999**, *103*, 7469−7479.
(62) Roberts, C. Molecular Sieves for Industrial Separation and Adsorption Applications. *The Properties and Applications of Zeolites*; 1980, *33*, 103.

https://doi.org/10.1021/acs.iecr.1c02261
Ind. Eng. Chem. Res. 2021, 60, 15236−15247